



THE UNIVERSITY *of* EDINBURGH

Edinburgh Research Explorer

The general circulation model precipitation bias over the southwestern equatorial Indian Ocean and its implications for simulating the South Asian monsoon

Citation for published version:

Bollasina, MA & Ming, Y 2013, 'The general circulation model precipitation bias over the southwestern equatorial Indian Ocean and its implications for simulating the South Asian monsoon', *Climate Dynamics*, vol. 40, no. 3-4, pp. 823-838. <https://doi.org/10.1007/s00382-012-1347-7>

Digital Object Identifier (DOI):

[10.1007/s00382-012-1347-7](https://doi.org/10.1007/s00382-012-1347-7)

Link:

[Link to publication record in Edinburgh Research Explorer](#)

Document Version:

Peer reviewed version

Published In:

Climate Dynamics

Publisher Rights Statement:

Author final draft as submitted for publication.

Cite As: Bollasina, MA & Ming, Y 2013, 'The general circulation model precipitation bias over the southwestern equatorial Indian Ocean and its implications for simulating the South Asian monsoon' *Climate Dynamics*, vol 40, no. 3-4, pp. 823-838.

Final publication copyright of Springer-Verlag (2013) available at link.springer.com

General rights

Copyright for the publications made accessible via the Edinburgh Research Explorer is retained by the author(s) and / or other copyright owners and it is a condition of accessing these publications that users recognise and abide by the legal requirements associated with these rights.

Take down policy

The University of Edinburgh has made every reasonable effort to ensure that Edinburgh Research Explorer content complies with UK legislation. If you believe that the public display of this file breaches copyright please contact openaccess@ed.ac.uk providing details, and we will remove access to the work immediately and investigate your claim.



The General Circulation Model Precipitation Bias over the Southwestern Equatorial Indian Ocean and its Implications for Simulating the South Asian Monsoon

Massimo A. Bollasina¹ and Yi Ming²

¹*Program in Atmospheric and Oceanic Sciences, Princeton University, Princeton*

²*Geophysical Fluid Dynamics Laboratory/NOAA, Princeton*

Submitted to *Climate Dynamics* on November 4, 2011; in revised form on January 16, 2012;
accepted on March 16, 2012.

Corresponding author:

Massimo A. Bollasina

Geophysical Fluid Dynamics Laboratory/NOAA

201 Forrestal Road

Princeton, NJ 08540

E-mail: massimo.bollasina@noaa.gov

Keywords: General circulation models; South Asian monsoon; sea surface temperature gradient; precipitation

ABSTRACT

Most of current general circulation models (GCMs) show a remarkable positive precipitation bias over the southwestern equatorial Indian Ocean (SWEIO), which can be thought of as a westward expansion of the simulated IO convergence zone toward the coast of Africa. The bias is common to both coupled and uncoupled models, suggesting that its origin does not stem from the way boundary conditions are specified.

The spatio-temporal evolution of the precipitation and associated three-dimensional atmospheric circulation biases is comprehensively characterized by comparing the GFDL AM3 atmospheric model to observations. It is shown that the oceanic bias, which develops in spring and reduces during the monsoon season, is associated to a consistent precipitation and circulation anomalous pattern over the whole Indian region. In the vertical, the areas are linked by an anomalous Hadley-type meridional circulation, whose northern branch subsides over northeastern India significantly affecting the monsoon evolution (e.g., delaying its onset).

This study makes the case that the precipitation bias over the SWEIO is forced by the model excess response to the local meridional sea surface temperature (SST) gradient through enhanced near-surface meridional wind convergence. This is suggested by observational evidence and supported by AM3 sensitivity experiments. The latter show that relaxing the magnitude of the meridional SST gradient in the SWEIO can lead to a significant reduction of both local and large-scale precipitation and circulation biases.

The ability of local anomalies over the SWEIO to force a large-scale remote response to the north is further supported by numerical experiments with the GFDL spectral dry dynamical core

model. By imposing a realistic anomalous heating source over the SWEIO the model is able to reproduce the main dynamical features of the AM3 bias.

These results indicate that improved GCM simulations of the South Asian summer monsoon could be achieved by reducing the springtime model bias over the SWEIO. Deficiencies in the atmospheric model, and in particular in the convective parameterization, are suggested to play a key role. Finally, the important mechanism controlling the simulated precipitation distribution over South Asia found here should be considered in the interpretation and attribution of regional precipitation variation under climate change.

1. Introduction

Atmospheric-only general circulation models (AGCMs) forced by observed SSTs [also known as Atmospheric Model Intercomparison Project (AMIP)-style runs] have been widely used to simulate and predict the South Asian summer monsoon (e.g., Sumi et al. 2005; Kang and Shukla 2006). Although these efforts have been generally successful in revealing mechanisms and processes over a broad range of temporal and spatial scales, a number of studies found that major shortcomings lead to the deterioration of the AGCMs performance over the monsoon region (e.g., Sperber and Palmer 1996; Gadgil and Sajani 1998; Kang et al. 2002; Kang et al. 2004; Wang et al. 2004, Krishna Kumar et al. 2005). Model skill is relatively poor even in basic quantities such as the seasonal mean precipitation distribution or its annual progression over South Asia (e.g., Kang and Shukla 2006). As one of the most important climate variables, precipitation is very difficult for AGCMs to simulate accurately. This is at least partly due to the models' reliance on highly parameterized physical processes, such as cumulus convection and large-scale condensation. As such, the analysis of simulated precipitation could shed light on the relative importance of these processes and the realism of their representations in models.

Several studies have emphasized the crucial role of coupled air-sea interactions in simulating the monsoon (e.g., Wu et al. 2006), highlighting the need for coupled atmosphere-ocean GCMs (AOGCMs; e.g., Krishna Kumar et al. 2005; Wang et al. 2005). This is especially true for regions where SSTs anomalies are driven at least in part by surface fluxes and wind stress (e.g., Lau and Nath 2000, Wu and Kirtman 2005). Nonetheless, it is challenging, even for AOGCMs, to simulate with fidelity the gross features of the South Asian monsoon (e.g., Annamalai et al. 2007; Bollasina and Nigam 2008).

Interestingly, some deficiencies in the simulated precipitation over South Asia are common to both AGCMs and AOGCMs, indicating that the underlying causes lie within the atmospheric component of the models (e.g., Meehl et al. 2006; Lin 2007; Kim and Kang 2008). For example, the coupling did not improve the models performance over large areas of the equatorial Indian Ocean (hereafter IO; e.g., Wu et al. 2006). Most AGCMs and AOGCMs substantially overestimate the observed climatological monsoon precipitation pattern over the equatorial IO (e.g., Gadgil and Sajani 1998; Fu et al. 2002; Kang et al. 2002; Bollasina and Nigam 2008; Rajeevan and Nanjundiah 2009). In view of these similarities between coupled and uncoupled models, the following investigation is mostly based on the “simpler” AGCMs.

Understanding the processes which lead to this large-scale precipitation anomaly may provide important insights into the factors controlling precipitation formation over the tropical IO (and, possibly, over other basins) and the associated large-scale ocean-atmosphere coupling in models. In particular, in an idealistic but useful view (e.g., Biasutti et al. 2006), the bias may originate from poorly simulated large-scale flow, which then provides unrealistic external forcing to regional-scale convection, or conversely from deficiencies in the parameterizations of specific processes (e.g., convection), which in turn influence the large-scale flow.

Broadly speaking, two main classes of theories relate tropical oceanic precipitation to SSTs (e.g., Biasutti et al. 2006; Sobel 2007; Back and Bretherton 2009). In one class, precipitation is determined by the local SSTs and related vertical profiles of temperature and humidity (“thermodynamic control”). In this view, low-level horizontal convergence is thought of as a mere response to the vertical motion induced by deep convective heating. In the other class, the low-level convergence of wind and moisture dictates the location and intensity of precipitation (“dynamic control”). The Planetary Boundary Layer (PBL) momentum budget defines the low-

level flow. Lindzen and Nigam (1987) suggested that local PBL pressure gradients result from differential heating associated with an underlying SST gradient. This theory may be particularly applicable to the IO, where the rather strong meridional SST gradient can be effective in driving the low-level convergence (e.g., Back and Bretherton 2009), especially in forcing the meridional component of the wind (e.g., Chiang et al. 2001). The role of PBL momentum dynamics in response to large cross-equatorial pressure gradients was for example suggested to be an important mechanism determining the location of the *actual* monsoon convection in the IO (Tomas and Webster 1997).

The primary motivation for this work is the observation that the large positive bias in model-simulated monsoon rainfall over the IO tends to coincide with a strong local meridional SST gradient. Moreover, this bias follows closely the rapid build-up of the meridional cross-equatorial SST gradient starting in early spring. The large-scale three-dimensional perspective adopted here allows for a comprehensive interpretation of the precipitation bias in the general framework of the monsoon circulation. This study suggests that AGCMs are overly sensitive to the *local* meridional SST gradient, thus giving rise to the overestimated precipitation over the western IO. The associated anomalous circulation causes appreciable biases elsewhere, most notably over South Asia.

The observational data, models, and numerical experiments used in this study are described in Section 2. The spatial and temporal evolution of the western tropical IO precipitation bias is described in Section 3. The relationship between the precipitation bias and the underlying SSTs distribution is examined in Section 4, providing empirical evidence for the SST dynamical control of local rainfall. The model sensitivity to the magnitude of the local meridional SST gradient is also investigated in a set of sensitivity experiments. In Section 5, we discuss the

impact of the precipitation anomaly over the IO on the simulated seasonal progression of the monsoon. Summary and conclusions follow in Section 6.

2. Observational Data and Models

2.1 Observational data

The European Centre for Medium-Range Weather Forecasts (ECMWF) Reanalysis (ERA-40; Uppala et al. 2005) provided monthly data at $2.5^\circ \times 2.5^\circ$ resolution and 6-hourly data on a 320×160 gaussian grid (about 1.125°). The 6-hourly data were averaged to pentads before being used in this study.

Precipitation observations came from the Global Precipitation Climatology Project (GPCP) version 2 (Adler et al. 2003) at pentad and monthly resolution, available on a $2.5^\circ \times 2.5^\circ$ grid from January 1979 onward. Monthly precipitation from the observation-only product of the Climate Prediction Center (CPC) Merged Analysis of Precipitation (CMAP) dataset (Xie and Arkin 1997) was also used to assess the robustness of the analysis. GPCP was chosen as the reference dataset. The main results and conclusions, however, would not be substantively altered by this choice. A third independent observational dataset was also considered: the Tropical Rainfall Measuring Mission (TRMM) 3B43 monthly precipitation at 0.25° resolution (Huffman et al. 2007). Although the TRMM data covers only the period January 1998-present, a 12-year climatology from this dataset was utilized for a closer examination of the details of the precipitation pattern.¹

¹ GPCP show a closer resemblance to TRMM than CMAP. Most notably, CMAP appears to have deficiencies over the Bay of Bengal and the eastern IO (e.g., Xie et al. 2006), with GPCP precipitation more anchored to the land (e.g., Cash et al. 2008).

Observed SSTs were from the Hadley Centre Sea Ice and Sea Surface Temperature dataset (HadISST; Rayner et al. 2003), a combination of global SST and sea ice concentration on a $1^\circ \times 1^\circ$ grid from 1870 to date.

2.2 Models

2.2.1 The GFDL Atmospheric Model AM3

The AM3 model is the atmospheric component of the new GFDL coupled atmosphere-ocean GCM CM3. It implements a prognostic representation of aerosol-cloud interactions, and interactive gas-phase chemistry and aerosol chemistry. Deep and shallow convections are parameterized separately. The horizontal resolution is $2^\circ \times 2.5^\circ$. There are 48 vertical levels, about half of which are in the troposphere [see Donner et al. (2011) for more details]. We analyze mainly a 21-year (1980-2000) simulation forced with observed monthly-varying SSTs and sea ice, excluding the first year as spin-up. AM3 is also used to perform a set of sensitivity experiments designed to study how a change in the meridional SST gradient over the western IO may affect the simulated rainfall.

2.2.2 The Dry Dynamical Core Model

This model consists of a time-marching spectral hydrostatic dynamical core and highly simplified forcing (Held and Suarez 1994). The horizontal resolution is T42, roughly equivalent to $2.8^\circ \times 2.8^\circ$, with 20 evenly-spaced vertical levels. A realistic orography, smoothed to the model resolution, is imposed. The specified three-dimensional diabatic heating is derived from the AM3 climatology. Temperature and winds are nudged toward their respective climatological values from the AM3 simulation. The Rayleigh drag is equivalent to a damping on a time scale

of 3 days at the surface, and decreases linearly to zero at $\sigma = 0.7$. The Newtonian cooling acts on a damping time scale of 40 days in the free atmosphere ($\sigma < 0.7$), decreasing to 1 day at the surface ($\sigma = 1$).

3. Spatio-temporal characteristics of the precipitation bias

3.1 Spatial pattern

The results described below are based on the analysis of AM3 and observations over the period 1981-2000 (20 years), referred to as the “climatology”. Figure 1 shows the observed April-May climatological precipitation and low-level winds over South Asia, as well as the AM3 relative biases (with GPCP as reference for precipitation). The observed climatological SSTs are also shown. Note that April and May correspond to the growing and mature phase of the large precipitation bias over the southwestern equatorial IO (hereafter SWEIO; see Fig. 2).

The IO is warmest in spring, with the 29°C isotherm approximately enclosing the area between 10°S and 15°N. With the development of the monsoon in June, the northern IO cools significantly due to the intense upwelling (e.g., Webster 2006). The spatial pattern of April-May SSTs is approximately zonal across the whole basin, with the strongest meridional gradient over the southern equatorial IO.

In all three observational datasets, the heaviest April-May precipitation occurs over the eastern equatorial IO, and it is accompanied by strong southeasterlies south of the equator. To its north, the southwesterly flow transports moisture across the Bay of Bengal and Indochina. Intense precipitation tends to be located over areas (i.e., the eastern IO) characterized by SSTs warmer than 27.5°C and by the presence of large-scale low-level convergence (e.g., Gadgil et al.

1984; Graham and Barnett 1987), with the latter playing the dominant role in governing convection for SST above the threshold (e.g., Graham and Barnett 1987; Gadgil 2003).

As a prominent model bias, AM3 overestimates precipitation, by a factor of two, over the central and western sections of the southern equatorial IO as a result of the simulated zonal rainbelt extending across the basin (Fig. 1d). This local bias is accompanied by other remarkable features over other parts of the IO and South Asia. They include the negative bias over the Bay of Bengal and Bangladesh, and the positive bias over much of India. The anomalous low-level flow shows well-defined structures as well. Two cyclonic circulations are present over the western IO, separated by strong equatorial westerlies. The one over the SWEIO is clearly associated with the local precipitation bias. Another important feature is an anticyclonic circulation centered over the Bay of Bengal, which opposes the climatological southwesterly wind.

To confirm that the AM3 biases are common also to other models, Figure 1e shows the biases in precipitation and 925-hPa winds from a multi-model average of five representative and widely used AGCMs (i.e., NCAR CAM3, Hadley HadGEM1, MPI ECHAM5, GFDL AM2.1, and CCSR/NIES/FRCGC MIROC3.2 hires) from the Intergovernmental Panel on Climate Change (IPCC) Fourth Assessment Report (AR4) archive. Magnitude and spatial pattern of these biases have a clear resemblance with the AM3 ones.

The fact that a similar bias is present in other AGCMs and AOGCMs (e.g., Gadgil and Sajani 1998; Kang et al. 2002; Bollasina and Nigam 2008)² indicates that the underlying causes are most likely due to deficiencies in the atmospheric models. Furthermore, the bias remains

² The analysis presented in Fig. 1e was also conducted with a multi-model average of Coupled Model Intercomparison Project phase 3 (CMIP3) GCMs, and with the GFDL coupled climate model CM3, of which AM3 is the atmospheric component. The biases in precipitation and low-level circulation, not displayed here for brevity, grossly resemble those of AM3, especially along the equatorial IO.

essentially the same when AM3 is forced with climatological SSTs (not shown), suggesting that it is rather constant from year to year.

3.2 Temporal evolution of the precipitation bias

The monthly evolution of the bias in precipitation and low-tropospheric winds from early spring to summer is represented in Fig. 2. The positive precipitation bias over the SWEIO appears first in March and then gradually migrates northward, while intensifying and expanding eastward until May. In June it moves further northward, but starts to decay. Concurrently, the magnitude of the negative bias over northeastern India, the northern Bay of Bengal, and southern China increases from March to June, and then decreases. Interestingly, this negative bias is largest in June, one month after the peak of the positive bias over the SWEIO. This hints at a possible causal relationship between the biases over the two areas, as will be discussed further in Section 5. Notably, the negative bias shows a very gradual decay through the summer months, much slower than the SWEIO precipitation bias. This negative bias appears to be linked to the westward positive bias over India through an anomalous zonal transverse closed circulation (not shown), opposing the climatology (e.g., Das 1962). We speculate that this circulation, reinforced by land-surface feedbacks over central India triggered by the increasingly excess moisture advected from the east (cf. Fig. 3), might be responsible for the longer persistence of the negative anomaly over the northern Bay of Bengal.

From March to May the low-level easterly wind anomalies show a progressive increase over the SWEIO, associated with an increase of the southwestward flow over Indochina and the Bay of Bengal and the formation of a cyclonic circulation over the northern Arabian Sea. From June,

the cyclonic flow over the Arabian Sea weakens and reverses, accompanied by a gradual weakening of the flow over the Maritime Continent.

The evolution of the *climatological* model bias and its changes in the meridional direction described above [in particular, the gradual precipitation increase (decrease) south (north) of 5°S and the development of a near-surface cyclonic circulation over the SWEIO during the growing phase] resemble the appearance of the asymmetric mode in the observed springtime rainfall and wind *interannual* variability described in Wu et al. (2008). The latter was shown to be initiated by a cross-equatorial SST gradient and to be modulated by regional air-sea interactions. As we will show, the evolution of the climatological model bias is also under heavy influence of these factors. These similarities suggest that the asymmetric pattern is an intrinsic mode of distribution for springtime precipitation and circulation over the IO.

4. Link between the precipitation bias and the meridional SST gradient

4.1 Low-level convergence

Considering the atmospheric water balance, the precipitation bias can be decomposed into two leading terms, vertically-integrated moisture flux convergence and evaporation. The total moisture flux is the sum of stationary and transient fluxes. Convergence from transient fluxes is, however, small over the south-equatorial IO ($\sim 0.5 \text{ mm day}^{-1}$, compared to $\sim 3 \text{ mm day}^{-1}$ from stationary fluxes using ERA-40 data) and can be neglected as a good first-order approximation. The evaporation bias is also modest ($\sim 1 \text{ mm day}^{-1}$). Figure 3 shows the model biases in the vertically-integrated stationary moisture flux convergence and in its main components for May. The bias in the convergence of stationary moisture fluxes (Fig. 3a) accounts for $\sim 90\%$ of the large precipitation positive bias over the SWEIO (50°-80°E, 15°-5°S). A further decomposition

of the stationary moisture flux convergence into its individual components (Fig. 3b) indicates that the bias in $-q \cdot \frac{\partial v}{\partial y}$ (the component due to the convergence of the meridional wind) is the single largest source of the overall bias in the stationary moisture flux convergence ($\sim 60\%$ of the column integrated amounts), especially due to the large overestimation in the lowest levels (below 850 hPa) where its spatial pattern closely mimics that of the precipitation bias (Fig. 3c). Figure 3b also shows that the terms related to the gradient of specific humidity are of secondary importance in the lower troposphere. The similarity between the spatial patterns of the biases in $-q \cdot \frac{\partial v}{\partial y}$ and $\frac{\partial v}{\partial y}$ (Fig. 3d) suggests that the former is mainly the result of an overestimation of the large-scale boundary layer wind meridional convergence.

The rapid decrease of the bias in $-q \cdot \frac{\partial v}{\partial y}$ in the lower troposphere deserves further investigation. At 850 hPa, the region of anomalous wind convergence (located in the 20° - 5° S band near the surface) shrinks in the meridional direction and a weak divergence appears over its southern part ($\sim 15^\circ$ S). Correspondingly, the vertical wind decelerates. Above 850 hPa the horizontal wind convergences again over the whole region and the vertical motion intensifies. These features reveal an interesting structure of the bias in the simulated vertical circulation: in the region of largest convergence, the near-surface layers are partially separated from the ones above 850 hPa by the existence of a low-level circulation below the major mid-tropospheric cell on the southern side. We will return to this issue later in Section 4.3.

4.2 Dynamical link with the SSTs

Figure 4 shows the time-latitude cross-section of the model biases in precipitation and sea level pressure (SLP) averaged over the western-central IO compared to observations. The excess precipitation in AM3 is tightly locked to the evolution of the underlying SSTs. The bias is placed over warm waters (i.e., above 27.5°C) and, as the isotherm moves northward, so does precipitation. Note, however, that the core of the bias is located over a region of large meridional SST gradient (cf. Fig. 1) and does not extend northward, where SSTs are warmer (but the gradient is weaker). Moreover, the precipitation bias increases as the warm pool develops north of the equator (increasing the SST gradient), and reduces as the waters in the northern IO cool (weakening the gradient but not the absolute value of SSTs over the anomalous precipitation region).

A dynamical link between SSTs and precipitation can be inferred from the analysis of the SLP bias (Fig. 4b). The simulated SLP shows a clear almost zonally-uniform bias with anomalous high (low) pressure centered at about 30°S (Equator) which adds up to the climatological pressure distribution (characterized by the Mascarene High centered at about 35°S) to generate an anomalous meridional (negative) SLP gradient. The zonal asymmetry of the SLP bias is negligible except close to the equator. Interestingly, the SLP bias evolves in concert with the imposed SST, with the largest negative (positive) pressure bias located over the warmest (coldest) SSTs. Note also that the bias in the simulated meridional SLP gradient increases from March to the peak in May at about 20°S (a region of rapidly varying SSTs), in association with the formation of the warmest SSTs to the north. Close to the equator the SLP bias is spatially more homogeneous, as the underlying SSTs.

Focusing for simplicity on May, the bias in the near-surface winds over the SWEIO can be largely explained in terms of the SLP bias and by considering the simplified three-way steady-state PBL momentum balance between the Coriolis acceleration, the pressure gradient, and friction (expressed as a Rayleigh drag) in the so-called Rayleigh Friction Model (e.g., Stevens et al. 2002; Back and Bretherton 2009). This approximate balance, which for example neglects the vertical mixing of momentum into the PBL, provides a reasonable description of the PBL winds. The winds are expressed as a sum of a geostrophic and a frictional component:

$$U = \frac{-\rho_o(fP_y + \varepsilon P_x)}{\varepsilon^2 + f^2}, \quad V = \frac{+\rho_o(fP_x + \varepsilon P_y)}{\varepsilon^2 + f^2}, \quad (1)$$

where U and V are the zonal and meridional wind components respectively, $P_x(P_y)$ is zonal (meridional) SLP gradient, f the Coriolis parameter, ρ_o a reference density, and ε the damping coefficient [$\sim(0.5-1 \text{ days})^{-1}$; Stevens et al. 2002]. Except in the proximity of the equator, f is always larger in magnitude than ε [for example, at 10°S $f \sim (2.2 \text{ days})^{-1}$] and the magnitude of the bias in P_y is much larger than that in P_x . In the $25^\circ\text{-}15^\circ\text{S}$ band, the simulated near-surface wind is slightly southeasterly as a result of the acceleration due to the meridional SLP gradient balanced mostly by the Coriolis force and, secondarily, by friction. Going north to about 10°S , both P_y and f decrease, and the wind is weaker and northeasterly as P_x is weak negative. In the $10^\circ\text{-}5^\circ\text{S}$ band, P_y (whose effect still dominates the balance) changes sign from positive to negative, and therefore both U and V reverses for a resulting northwesterly wind. The gradual reversal of the meridional component of the wind from positive at $\sim 20^\circ\text{S}$ to negative at $\sim 5^\circ\text{S}$ thus generates an anomalous meridional convergence (cf. Fig. 3) which, based on the above analysis, is in large part attributable to the meridional SLP gradient. A result of the forced convergence and development of convection is the removal of mass from the PBL by cumulus mass flux.

Indeed, the model largely underestimates the PBL height across the whole south-equatorial IO (cf. Section 4.3; Medeiros et al. 2005)³, with maximum decrease (-350 m) over the SWEIO.

In summary, the major features of the model bias in low-level convergence over the SWEIO and of its temporal variation appears to be linked to the underlying meridional SST gradient and its driven SLP distribution [i.e., through a mechanism as in Lindzen and Nigam (1987)].

4.3 Impact of the SST gradient: numerical experiments

The link between the simulated regional precipitation bias and the imposed meridional SST gradient over the SWEIO is investigated by means of two experiments, each consisting of a 3-member ensemble of May simulations with AM3. In the control run (IDEAL), the actual climatological SSTs between 40°-80°E (where the largest precipitation bias is located; see Fig. 2) and in the latitude range 35°S-20°N are zonally-averaged and replaced by a Gaussian fit.⁴ In the sensitivity experiment (IDEAL_R), the parameters of the Gaussian fit are altered to reduce the meridional SST gradient by 20% in the latitudinal band 5°-23°S, which delimits the area of the targeted precipitation bias (Fig. 5a). Note that the SST change north of 5°S (where climatological SSTs are warmer) is negligible (less than 0.2°C on the 5°S-25°N average SST). In particular, note that the impact of modified SSTs absolute values on precipitation would actually work against the expected effect due to a modified SST gradient. For example, a reduction of the SST gradient south of 5°S should decrease surface convergence and therefore precipitation; at

³ Since global observations of PBL height are not available, the ERA40 PBL is used as “observations” for this qualitative analysis. von Engel and Texeira (2010) estimate a springtime PBL height of about 1250 m over the SWEIO, comparable to the ~1000 m from the ERA40 climatology. Both estimates are much higher than the AM3 values (~600 m).

⁴ The average SST values between 35°S-20°N are 26.97°C and 27.03°C for the idealized and actual profiles, respectively, while the root mean square difference is 0.54°C. South of 35°S a relatively abrupt transition between the idealized and actual SST profiles exists, which could be smoothed out. At this time, this critical latitude was considered to be located sufficiently southward of the targeted precipitation region to avoid any substantial impact on the area of interest, given the preliminary and mostly qualitative nature of these experiments.

the same time, it also results in increased average SSTs there, which should favor convection. It follows that these experiments will *conservatively* suggest the predominance of either control mechanisms on simulated precipitation over the region.

Figure 5b shows the bias of the IDEAL experiment in precipitation and 925-hPa circulation, to be compared to Fig. 2c. The two maps are very similar, confirming that the current set-up and the use of the idealized SSTs distribution do not significantly alter the performance of the model compared to the AMIP-style run.

The reduction of the meridional SST gradient substantially modifies the precipitation distribution and the flow over the whole basin (Fig. 5c). The black dots in Fig. 5c mark the grid points for which the difference in precipitation exceeds the 90% significance level according to the two-tailed Student's *t*-test on the difference of the averages of two independent populations with unequal variances (e.g., Helsel and Hirsch 2002). Despite the associated increase in the absolute SSTs values, precipitation between 10°S and the equator, largely overestimated in IDEAL, is significantly reduced by more than 50% in IDEAL_R. Large-scale precipitation, whose contribution to the total precipitation is in general negligible compared to the convective fraction in IDEAL, is found to equally contribute to the reduction in the band 10°-5°S. The positive bias in the Arabian Sea and over India is largely reduced too (more than 50%). On the other hand, precipitation increases over large areas of Indochina, the Maritime continent and southern China, where IDEAL was overall drier than observations. These results further support the existence of a remote forcing from the SWEIO, which will be more directly investigated in the following section.

The SST gradient has also a clear impact on the circulation bias: the two low-level cyclones over the Arabian Sea are replaced by anticyclones, and the northeasterly flow across Indochina

and the Bay of Bengal by southwesterlies. The meridional circulation reverses, and anomalous subsidence occurs south of the equator. Interestingly, a secondary shallow lower-tropospheric circulation appears between 10°-20°S (over relatively cold SSTs; not shown) beneath the deeper upper-tropospheric circulation, as also found by Larson and Hartmann (2003). Several studies have discussed the presence of a secondary, low-level circulation in regions of strong (zonal) SST-gradient forcing (e.g., Grabowski et al. 2000; Nolan et al. 2007).

Decreasing the meridional SST gradient leads also to a general local decrease of relative humidity and low and middle clouds amounts (not shown; e.g., Larson and Hartmann 2003), as well as to a reduction of the cumulus mass flux, which contributes to increasing the PBL height.

5. Link with the large-scale circulation

5.1 Large-scale circulation biases

To obtain a large-scale perspective of the impact of the precipitation bias over the IO on the simulation of the regional atmospheric circulation, the 200-hPa divergent circulation for May is analyzed in Fig. 6. Note that the outflow from tropical deep convection is typically located at 200 hPa. In May, the largest observed climatological divergence is located over the Maritime Continent and extends across the equatorial IO to the west and Indochina to the north (Fig.6a). The divergent flow converges mainly over two regions, namely northwestern India and the Middle East in the northern hemisphere and over the Mascarene High in the southern hemisphere. Consistently with the precipitation bias (cf. Fig. 2), the model simulates anomalous ascent and upper-level divergence over the SWEIO, with one branch of the outflow heading northward and converging (Fig. 6b). A wide convergence area encompasses northeastern India, Indochina, and part of the Bay of Bengal, where anomalous subsidence opposes the

climatological ascent, reducing precipitation. Anomalous upper-level convergence is located also over northwestern India, which reinforces the climatological subsidence over this dry region. The sector-averaged anomalous meridional circulation can be perceived as a direct Hadley-type circulation linking the divergent outflow over the SWEIO with subsidence and deficient precipitation to the north.

The time-latitude cross-section of the bias in the 200-hPa divergent circulation is shown in Fig. 6c. Data have been averaged over the central IO to enclose both the ascent area over the IO and the descent over the continent. Consistently with the evolution of the precipitation bias, the anomalous outflow over the SWEIO intensifies from March and moves northward, accompanied by the increase of anomalous convergence to the north in June.

5.2 Impact on the South-Asian monsoon onset

It is perceivable that anomalous subsidence over northeastern India caused by the positive precipitation bias over the SWEIO could affect the northwestward migration of convection from Indochina, and thus the timing of the summer monsoon onset (e.g., Ramage 1971). Although the monsoon onset normally refers to the abrupt increase of rainfall, it is also accompanied by relatively sharp shifts in the dynamical and thermodynamical characteristics of the large-scale circulation over South Asia and the Indian Ocean. Two most noticeable aspects are the rapid acceleration of the low-level southwesterly winds over the Arabian Sea (e.g., Goswami 2005), and the reversal of the meridional temperature gradient in the upper troposphere south of the Tibetan Plateau (e.g., Li and Yanai 1996; Webster et al. 1998).

The pentad evolution of the model biases in these three quantities from late spring to early summer is represented in Fig. 7. Observations are also displayed to make the analysis easier.

Precipitation and upper-level temperature are zonally averaged over the Indian monsoon region, while the 850-hPa zonal wind is averaged over the core of the Somali jet. The observed sudden increase of precipitation north of about 10°N in early June is clearly misrepresented in AM3, as simulated precipitation intensifies considerably only in the second half of June (Fig.7a). The arrival of the monsoon rains over the Indian sector appears therefore to be delayed approximately by 2 pentads. Annamalai et al. (2005) also found a comparable delay in the atmospheric response to positive precipitation anomalies over the SWEIO induced by local anomalously-warm SSTs. Once established, the monsoon remains stronger than in observations, especially during the mature phase.

Similarly, the simulated low-level wind over the Arabian Sea (which brings moisture toward India) intensifies only in the second half of June, favored by the weakening of the anomalous cyclonic circulation (cf. Fig. 2), and leading to the so-called “dynamical” onset of the monsoon (Fig. 7b).

The tropospheric thermal structure at the monsoon onset is well depicted by the 200-500-hPa layer mean temperature (Fig. 7c): an elevated warm core forms over South Asia resulting in a strong temperature meridional gradient (e.g., Webster 2006). Climatologically, positive temperature anomalies begin to appear in early May at 30°N , reaching maximum values ($>9^{\circ}\text{C}$) in July in the 60° - 105°E sector. In the same region, the simulated upper tropospheric heating is gradual and weaker than in observations and peaks in the middle of June.

In summary, the similarity in the evolution of these variables depicts a dynamically and thermodynamically consistent picture of the delay in the simulated monsoon onset.

5.3 Large-scale impact of anomalous heating: numerical experiments

The GFDL dry dynamical core model is used to investigate the development and evolution of the large-scale circulation response to the positive precipitation bias and associated anomalous latent heating over the SWEIO. We choose to focus on the month of May partly because the bias is largest. Moreover, since May effectively sets up the stage for the South Asian monsoon onset, which occurs in early June, we pay special attention to the possible impact on the simulation of the large-scale monsoon flow. A control simulation, driven by the diabatic heating computed in AM3, is compared to a sensitivity case in which the heating over the SWEIO (50° - 80° E, 5° - 15° S) is reduced by 30% uniformly at all levels (see Fig. 8a). The heating perturbation is approximately equivalent to a maximum precipitation decrease of about 2.8 mm day^{-1} , which is comparable to the AM3 precipitation bias during May over the same region ($\sim 3.6 \text{ mm day}^{-1}$).⁵

Figure 8 summarizes the key results of the numerical experiments in terms of forced response to a *positive* diabatic heating anomaly (i.e., the difference control minus sensitivity case), which can be compared to the AM3 bias. The response develops instantly over the SWEIO and propagates across the globe in about a week, establishing a distinct wave pattern. As previously discussed (e.g., Jin and Hoskins 1995; DeWeaver and Nigam 2004), baroclinically unstable waves tend to grow over time, and dominate the solution after typically 12-15 days. In our experiments, such unstable waves start to take hold after day 10 (see Fig. 8f).

The left column of Fig. 8 (Figs. 8a, c, e) shows the 174-hPa streamfunction and the 524-hPa pressure-vertical velocity (positive downward) anomalies at three time steps ($t = 2, 6$, and 10 days). The anomalous diabatic heating rapidly leads to strong ascent and upper-tropospheric

⁵ A control and an “additional heating” experiments were also performed with a steady, linear primitive equation model (Bollasina and Nigam 2011) forced by ERA-40 climatological mean fields, including three-dimensional diabatic heating. The “additional heating” experiment consisted in prescribing a positive diabatic heating anomaly over the SWEIO mimicking the AM3 precipitation bias during May. The simulated equilibrium response is consistent with the dry dynamical model response at $t=10$ days.

divergence locally over the SWEIO, while exciting a south-equatorial anticyclonic (cyclonic) circulation to the west (east) at day 2. The former conforms to the equatorially trapped Rossby wave response. The substantial asymmetry of the heating with respect to the equator results in the disappearance of the eastward Kelvin wave (e.g., Rodwell and Hoskins 1996). The northern branch of the westward equatorial Rossby wave, in the form of an anticyclonic circulation north of the equator, appears at day 3 (not shown), and it is weaker than its south-equatorial counterpart due to the characteristic form of the mean flow.⁶ The northern hemisphere anticyclone continues to develop and extends westward, and by day 6 stretches over part of east Africa, the Middle East and the eastern Mediterranean. To the east of the heating, Rossby wave trains develop in both hemispheres and propagate toward the subtropics and middle latitudes by overcoming the equatorial easterlies. By day 10, the stronger southern branch has become an eastward wave train across the globe, while the northern branch extends to about the dateline. The former is associated with descent over the southeastern IO and ascent over the Maritime Continent. The latter gives rise to an upper-level cyclonic circulation over northwestern India, with associated widespread descent over northern India, Indochina and the Bay of Bengal, and ascent over Peninsular India and the northern Arabian Sea toward Pakistan (Fig. 8e). Correspondingly, the upper-level meridional wind is northerly (southerly) over western India (Indochina), in agreement with the Sverdrup balance (Fig. 8b). Although other factors aside the forcing from the SWEIO contribute to generating the AM3 regional precipitation and circulation biases (e.g., remote forcing from other regions), the qualitative similarity between the circulation anomalies displayed in Fig. 8 and the AM3 circulation biases (Figs. 2, 6) is nonetheless

⁶ The mean flow plays an important role in determining the growth and propagation of waves from the perturbed region. During May upper-level weak easterlies ($\sim 5\text{--}10\text{ m s}^{-1}$) lie over the region of the prescribed heating and northward to about 10°N , which tend to dampen the amplitude of the Rossby wave response. However, the strong westerlies ($\sim 25\text{ m s}^{-1}$) over northern India facilitate the growth of Rossby waves.

noteworthy. For example, the remotely-forced pattern of vertical motion associated with the important precipitation bias over the continent and nearby ocean is reasonably well reproduced (i.e., subsidence over northern India, Bay of Bengal, and Indochina, and ascent over Peninsular India and the Arabian Sea). These results support the hypothesis of an important remote influence of SWEIO anomalous condensational heating on the large-scale circulation over the Indian subcontinent (see also Annamalai et al. 2005).

Further insights into the model solution are provided by Fig. 8d and f, which portrays some characteristics of the meridional wind (e.g., Jin and Hoskins 1995). The vertical structure of the northern wave train is shown by the cross-section of the meridional wind at day 10 and averaged between 26.5° - 35° N, which crosses the region of interest (Fig. 8d). There is strong equivalent barotropic component, in the sense that variations in wind (or geopotential height) have the same sign at all levels, with maximum change at the upper levels. The longitude-time plot of the 174-hPa meridional wind at 30° N (Fig. 8f) indicates that the northern hemisphere wave train develops after about 5 days and persists for another 5 days (with an eastward phase speed) before being overwhelmed by baroclinically unstable waves.

6. Summary and Conclusions

This work was motivated by the need for a better understanding of the spatiotemporal characteristics and mechanism leading to the large positive precipitation bias over the southwestern equatorial IO during spring-to-summer in most of current GCMs. This bias, which can be thought of as a westward expansion of the simulated IO tropical convergence zone toward the coast of Africa, clearly stands out as a remarkable shortcoming of the simulated monsoon. Its presence is pervasive across both uncoupled and coupled models, and, in the former case, it is

not sensitive to the specification of actual or climatological SSTs. This indicates that the bias is most likely a consequence of the physical parameterizations currently employed in GCMs.

This study makes the case for a strong control of the meridional SST gradient in the western IO on the simulated distribution of precipitation. A detailed examination of the spatiotemporal evolution of the regional precipitation and three-dimensional atmospheric circulation biases in the GFDL AM3 provides evidence that the model convection is controlled by the latitudinal SST gradient. The latter hydrostatically induces a meridional pressure gradient, which in turn affects the near-surface wind convergence and leads to local precipitation development (e.g., Lindzen and Nigam 1987). The local bias over the IO is shown to induce consistent large-scale precipitation and circulation biases over South Asia by forcing a meridional Hadley-type circulation across the equator, with a remotely-forced descending branch over northeastern India/Indochina. As a result, the simulated South Asian monsoon has a more gradual onset over India. The case is further supported by sensitivity experiments with AM3. By relaxing the imposed SST gradient over the southwestern equatorial IO, the model is able to substantially recover from all the major deficiencies of its control simulation over South Asia. This attests to the importance of the near-surface SST-gradient forcing and the existence of shortcomings in the representation of related processes in determining a large-part of the regional model bias. The AM3 simulation shows that through a modification of the lower-tropospheric circulation, important changes are induced also in the simulated clouds, convection, and diabatic heating across the equatorial IO.

The large-scale changes in the model simulation brought about by its sensitivity to the magnitude of the local SST-gradient represent a current serious deficiency in the portrayal of the monsoon circulation, which significantly hampers our understanding of regional processes and

feedbacks even with respect to the mean annual cycle. In this respect, one immediate conclusion is that deficiencies in simulating springtime climate affect the overall performance of the model through the subsequent monsoon season. In particular, a realistic representation of local air-sea interactions over the SWEIO is crucial for a skillful simulation of the South Asian summer monsoon. In other words, surface forcing over the SWEIO plays a key role in determining the seasonal evolution of regional hydroclimate as depicted by current GCMs.

This bias affects also the reliability of current projections of future regional precipitation distribution, especially considering that the meridional SST gradient over the SWEIO (and thus its anomalous forcing in the models) is projected to strengthen in a warming climate (e.g., Ihara et al. 2009; Xie et al. 2010). For the same reason, it is however also possible that in the future the forcing mechanism might become more relevant also in the real world. Furthermore, the modulation of the summertime meridional SST gradient from aerosol-reduced incidence of shortwave radiation over the northern IO has been deemed responsible for the drying trend of the South Asian monsoon over India (e.g., Chung and Ramanathan 2006). We speculate that an important contribution to the continental aerosol effect (mediated by the modification of the *large-scale* SST pattern in the northern IO) is attributable to the model response to the reduced *local* gradient in the south-equatorial IO through *local* processes. An understanding of the models biases and of the role of air-sea interactions over the SWEIO are therefore crucial for the analysis and interpretation of regional climate change scenarios (e.g., Copsey et al. 2006).

One may ask if the ocean-atmosphere coupling has any effect on the precipitation bias. As noted above, the major spatial characteristics and seasonal evolution of the bias are common to both coupled and uncoupled models, with comparable precipitation amounts over the SWEIO. North of the equator, springtime oceanic precipitation in coupled models tends to be slightly

underestimated (not only in the Bay of Bengal as for the AGCMs), likely due to additional subsidence originating from excess precipitation over the Maritime continent/western Pacific which calls for an important role of *non-local* forcing (e.g., Wu et al. 2006; Wu and Kirtman 2007). An examination of other variables suggests the existence of a strong feedback of the atmosphere on the ocean, given for example the association of the drying in the 0°-10°N band with weaker surface winds, reduced evaporation, and warmer SSTs (e.g., Lin 2007). Clearly this mechanism cannot be represented in AGCMs.

A detailed investigation into the model physics to identify possible parameters which may alleviate the model bias would be the natural extension of this work. Interestingly, the results described here may be useful to improve our understanding of the simulation of other tropical phenomena. A systematic relationship between intraseasonal variability (ISV) and mean state bias in AGCMs has been discussed in several studies (e.g., Sperber and Annamalai 2008; Kim et al. 2011). In particular, there is an evident resemblance between the precipitation bias found here and the composite strong-ISV minus weak-ISV models in Kim et al. (2011), especially the locking of precipitation over the south-equatorial IO in weak-ISV models (their Fig. 2) and the southwest-northeast dipole (their Fig. 7). The sensitivity of their results to the convection entrainment rate may also work in this context. PBL forced-convergence and ascent moisten the free troposphere, which in turn reduces the efficiency of entrainment in preventing the development of deep convection (e.g., Sobel 2007).

Acknowledgements

The authors would like to thank Chris Golaz for helpful discussions. We also thank Takeshi Doi and Matthew Harrison for reviewing an earlier version of the manuscript, as well as two anonymous reviewers for their comments.

References

- Adler RF., Huffman GJ, Chang A, Ferraro R, Xie P, Janowiak J, Rudolf B, Schneider U, Curtis S, Bolvin D, Gruber A, Susskind J, Arkin P, Nelkin E (2003) The version 2 Global Precipitation Climatology Project (GPCP) monthly precipitation analysis (1979-Present). *J Hydrometeor* 4: 1147-1167
- Annamalai H, Liu P, Xie SP (2005) Southwest Indian ocean SST variability: its local effect and remote influence on Asian monsoons. *J Clim* 18: 4150–4167
- Annamalai H, Hamilton K, Sperber KR (2007) South Asian summer monsoon and its relationship with ENSO in the IPCC AR4 simulations. *J Clim* 20: 1071–1092
- Back LE, Bretherton CS (2009) On the relationship between SST gradients, boundary layer winds and convergence over the tropical oceans. *J Clim* 22: 4182-4196
- Biasutti M., Sobel AH, Kushnir Y (2006) AGCM precipitation biases in the tropical Atlantic. *J Clim* 19: 935-958
- Bollasina M., Nigam S (2008) Indian Ocean SST, evaporation, and precipitation during the South Asian summer monsoon in IPCC-AR4 coupled simulations. *Clim Dyn* 33: 1017-1033
- Bollasina M, Nigam S (2011) The summertime “heat” low over Pakistan/northwestern India: evolution and origin. *Clim Dyn* 37: 957-970
- Cash BA, Rodo X, Kinter JL, Fennessy MJ, Doty B. (2008) Differing estimates of observed Bangladesh summer rainfall. *J Hydromet* 9: 1106–1114
- Chiang JCH., Zebiak SE, Cane MA (2001) Relative roles of elevated heating and surface temperature gradients in driving anomalous surface winds over tropical oceans. *J Atmos Sci* 58: 1371-1394

- Chung CE, Ramanathan V (2006) Weakening of North Indian SST gradients and the monsoon rainfall in India and the Sahel. *J Clim* 19: 2036-2045
- Copsey D, Sutton R, Knight JR (2006) Recent trends in sea level pressure in the Indian Ocean region. *Geophys Res Lett* 33: L19712, doi:10.1029/2006GL027175
- Das PK (1962) Mean vertical motion and non-adiabatic heat sources over India during the monsoon. *Tellus* 14: 212–220
- DeWeaver ET, Nigam S (2004) On the forcing of ENSO teleconnections by anomalous heating and cooling. *J Clim* 17: 3225-3235
- Donner LJ, and Coauthors (2011) The dynamical core, physical parameterizations, and basic simulation characteristics of the atmospheric component AM3 of the GFDL Global Coupled Model CM3. *J Clim* 24: 3484–3519
- Fu X, Wang B, Li T (2002) Impacts of air–sea coupling on the simulation of mean Asian summer monsoon in the ECHAM4 model. *Mon Wea Rev* 130: 2889–2904
- Gadgil S, Joseph PV, Joshi NV (1984) Ocean atmosphere coupling over monsoon regions. *Nature* 312:141–43
- Gadgil S, Sajani S (1998) Monsoon precipitation in the AMIP runs. *Clim Dyn* 14: 659-689
- Gadgil S (2003) The Indian monsoon and its variability *Annu Rev Earth Planet Sci* 2003. 429–67.
- Goswami BN (2005) South Asian summer monsoon: an overview. *The Global Monsoon System: Research and Forecast*, C.-P. Chang, B. Wang, and N.-C. G. Lau (Eds.), WMO/TD No. 1266 (TMRP Report No. 70), 47–71
- Grabowski WW, Yano JI, Moncrieff MW (2000) Cloud resolving modeling of tropical circulations driven by large-scale SST gradients. *J Atmos Sci* 57: 2022–2040

- Graham N, Barnett TP (1987) Sea surface temperature, surface wind divergence, and convection over tropical oceans. *Science* 238: 657–659
- Held IM, Suarez MJ (1994) A proposal for the intercomparison of the dynamical cores of atmospheric general circulation models. *Bull Amer Meteor Soc* 73: 1825-1830
- Helsel DR, Hirsch RM (2002) *Statistical Methods in Water Resources Techniques of Water Resources Investigations, Book 4, chapter A3*. U.S. Geological Survey. 522 pages (available at the web address: <http://pubs.usgs.gov/twri/twri4a3/>).
- Huffman GJ, Adler RF, Bolvin DT, Gu G, Nelkin EJ, Bowman KP, Hong Y, Stocker EF, Wolff DB (2007) The TRMM Multisatellite Precipitation Analysis (TMPA): quasi-global, multiyear, combined-sensor precipitation estimates at fine scales. *J Hydrometeor* 8: 38–55
- Ihara C, Kushnir Y, Cane MA, de la Peña VH (2009) Climate change over the equatorial Indo-Pacific in global warming. *J Clim* 22: 2678–2693
- Jin FF, Hoskins BJ (1995) The direct response to tropical heating in a baroclinic atmosphere. *J Atmos Sci* 52: 307–319
- Kang IS, et al (2002) Intercomparison of the climatological variations of Asian summer monsoon precipitation simulated by 10 GCMs. *Clim Dyn* 19: 383-395
- Kang IS, Lee JY, Park CK (2004) Potential predictability of summer mean precipitation in a dynamical seasonal prediction system with systematic error correction. *J Clim* 17: 834-844
- Kang IS, Shukla J (2006) Dynamical seasonal prediction and predictability of the monsoon. *The Asian Monsoon*, B. Wang (Ed.), Praxis Pub. Ltd., Chichester, UK, 585-612
- Kim HM, Kang IS (2008) The impact of ocean–atmosphere coupling on the predictability of boreal summer intraseasonal oscillation. *Clim Dyn* 31: 859–870

- Kim D, Sobel AH, Maloney ED, Frierson DMW, Kang IS (2011) A systematic relationship between intraseasonal variability and mean state bias in AGCM simulations. *J Clim* 24: 5506-5520
- Krishna Kumar K., Hoerling M, Rajagopalan B (2005) Advancing dynamical prediction of Indian monsoon rainfall. *Geophys Res Lett* 32: L08704, doi:10.1029/2004GL021979
- Larson K, Hartmann DL (2003) Interactions among cloud, water vapor, radiation, and large-scale circulation in the tropical climate. Part II: sensitivity to spatial gradients of sea surface temperature. *J Clim* 16: 1441-1455
- Lau NC, Nath MJ (2000) Impact of ENSO on the variability of the Asian–Australian monsoons as simulated in GCM experiments. *J Clim* 13: 4287–4309
- Li C., Yanai M (1996) The onset and interannual variability of the Asian summer monsoon in relation to land-sea thermal contrast. *J Clim* 9: 358-375
- Lin JL (2007) The double-ITCZ problem in IPCC AR4 coupled GCMs: ocean-atmosphere feedback analysis. *J Clim* 20: 4497-4525
- Lindzen RS, Nigam S (1987) On the role of sea surface temperature gradients in forcing low level winds and convergence in the tropics. *J Atmos Sci* 44: 2418-2436
- Medeiros B, Hall A, Stevens B (2005) What controls the mean depth of the PBL? *J Clim* 18: 3157–3172
- Meehl GA, Arblaster JM, Lawrence DM, Seth A, Schneider EK, Kirtman BP, Min D (2006) Monsoon regimes in the CCSM3. *J Clim* 19: 2482–2495
- Nolan DS, Zhang C, Chen SH (2007) Dynamics of the shallow meridional circulation around intertropical convergence zones. *J Atmos Sci* 64: 2262–2285

- Rajeevan M, Nanjundiah RS (2009) Coupled model simulations of twentieth century climate of the Indian summer monsoon. In Platinum Jubilee Special Volume of the Indian Academy of Sciences, Indian Academy of Sciences, Bangalore, pp. 537–568
- Ramage CS (1971) Monsoon Meteorology. Academic Press, New York, 296pp
- Rayner NA, Parker DE, Horton EB, Folland CK, Alexander LV, Rowell DP, Kent EC, Kaplan A (2003) Global analyses of sea surface temperature, sea ice, and night marine air temperature since the late nineteenth century. *J Geophys Res* 108: 4407 10.1029/2002JD002670
- Rodwell MJ, Hoskins BJ (1996) Monsoons and the dynamics of deserts. *Q J R Met Soc* 122: 1385-1404
- Sobel AH (2007) Simple models of ensemble-averaged precipitation and surface wind, given the SST. *The Global Circulation of the Atmosphere*, T. Schneider and A. H. Sobel (Eds.), Princeton University Press, 219-251
- Sperber KR, Palmer T (1996) Interannual tropical rainfall variability in general circulation model simulations associated with the Atmospheric Model Intercomparison Project. *J Clim* 9: 2727-2750
- Sperber KR, Annamalai H (2008) Coupled model simulations of boreal summer intraseasonal (30–50 day) variability, Part 1: Systematic errors and caution on use of metrics. *Clim Dyn* 31: 354-372
- Stevens B, Duan J, McWilliams JC, Munnich M, Neelin JD (2002) Entrainment, Rayleigh friction and boundary layer winds over the Tropical Pacific. *J Clim* 15: 30-44
- Sumi A, Lau NC, Wang WC (2005) Present Status of Asian Monsoon Simulation. *The Global Monsoon System: Research and Forecast*, C.-P. Chang, B. Wang, and N.-C. G. Lau (Eds.), WMO/TD No. 1266 (TMRP Report No. 70), 376–385

- Tomas R, Webster PJ (1997) On the location of the intertropical convergence zone and near-equatorial convection: The role of inertial instability. *Q J R Met Soc* 123: 1445-1482
- Uppala SM, et al (2005) The ERA40 reanalysis. *Q J R Met Soc* 131: 2961-3012
- von Engeln A, Teixeira J (2010) A planetary boundary layer height climatology derived from ECMWF Re-analysis data. *J Appl Met Clim* (submitted)
- Wang B, Kang IS, Li JY (2004) Ensemble simulation of Asian-Australian monsoon variability by 11 AGCMs. *J Clim* 17: 803-818
- Wang B, Ding Q, Fu X, Kang IS, Jin K, Shukla J, Doblas-Reyes F (2005): Fundamental challenge in simulation and prediction of summer monsoon rainfall. *Geophys Res Lett* 32: L15711, doi:10.1029/2005GL022734
- Webster PJ, Magana VO, Palmer TN, Shukla J, Tomas RA, Yanai M, Yasunari T (1998) Monsoons: Processes, predictability, and the prospects for prediction *J Geophys Res* 103: 14451-14510
- Webster PJ (2006) The coupled monsoon system. *The Asian Monsoon*, B. Wang (Ed.), Praxis Pub. Ltd., Chichester, UK, 3-66
- Wu R, Kirtman BP (2005) Roles of Indian and Pacific Ocean air-sea coupling in tropical atmospheric variability. *Clim Dyn* 25: 155-170
- Wu R, Kirtman BP (2007) Regimes of seasonal air-sea interaction and implications for performance of forced simulations. *Clim Dyn* 29: 393-410
- Wu R, Kirtman BP, Pegion K (2006) Local air-sea relationship in observations and model simulations. *J Clim* 19: 4914-4932
- Wu R, Kirtman BP, Krishnamurthy V (2008) An asymmetric mode of tropical Indian Ocean rainfall variability in boreal spring. *J Geophys Res* 113: D05104, doi:10.1029/2007JD009316

- Xie P, Arkin PA (1997) Global precipitation: A 17-year monthly analysis based on gauge observations, satellite estimates, and numerical model outputs. *Bull Amer Meteor Soc* 78: 2539-2558
- Xie SP, Xu H, Saji NH, Wang Y, Liu WT (2006) Role of narrow mountains in large-scale organization of Asian monsoon convection. *J Clim* 19: 3420–3429
- Xie SP, Deser C, Vecchi GA, Ma J, Teng H, Wittenberg AT (2010) Global warming pattern formation: sea surface temperature and rainfall. *J Clim* 23: 966–986

Figure captions

Figure 1: April-May average of: (a) GPCP precipitation (mm day^{-1}) and SST ($^{\circ}\text{C}$); (b) CMAP precipitation (mm day^{-1}) and ERA-40 925-hPa winds (m s^{-1}); (c) TRMM 3B43 precipitation (mm day^{-1}); (d) AM3 biases in precipitation (shaded, mm day^{-1} ; with GPCP as reference) and 925-hPa winds (vectors, m s^{-1}), with the simulated precipitation (mm day^{-1}) as black contours; (e) As (d) but for a multi-model average of five representative AGCMs (i.e., NCAR CAM3, Hadley HadGEM1, MPI ECHAM5, GFDL AM2.1, and CCSR/NIES/FRCGC MIROC3.2 hires) from the IPCC-AR4 archive. All data in (a)-(d) are 1981-2000 mean values, except TRMM which covers the period 1998-2009. Data in (e) are for 1981-1999.

Figure 2: Monthly evolution of the AM3 bias in precipitation (mm day^{-1} , shaded) and 925-hPa winds (m s^{-1} ; vectors plotted only when the magnitude of the wind bias exceeds 1.5 m s^{-1}) from March (a) to August (f).

Figure 3: May climatological (a) AM3 bias in precipitation (P , mm day^{-1} , contour) and 1000-300 hPa vertically integrated stationary moisture flux convergence (MFC, mm day^{-1} , shaded); (b) vertical profiles of the AM3 biases (s^{-1}) in various components contributing to the stationary moisture flux convergence averaged over the area (50° - 80°E , 15° - 5°S); (c) AM3 bias in the 1000-850 hPa vertically integrated meridional moisture transport (mm day^{-1}); (d) AM3 bias in the 1000-850-hPa average convergence of the meridional wind ($\times 10^6 \text{ s}^{-1}$). In these panels, q is specific humidity, v the meridional component of the wind, u the zonal component of the wind, y the latitude, and x the longitude.

Figure 4: (a): Latitude-time plot of monthly observed GPCP precipitation (mm day^{-1} , shaded), sea level pressure (hPa, black contours), and SST ($^{\circ}\text{C}$, green contours) averaged over the oceanic grid-points between 50° - 80°E . (b): as in (a) but for the AM3 bias in precipitation (mm day^{-1} , shaded) and sea level pressure (hPa, black contours).

Figure 5: (a): Latitudinal variation of the 50° - 80°E average observed May climatological SST (CLIM, black), its Gaussian fit (IDEAL, green), and the Gaussian fit after a 20% reduction of the latitudinal gradient between 23° - 5°S (IDEAL_R, blue). (b): AM3 bias in precipitation (shaded, mm day^{-1}) and in 925-hPa winds (streamlines) when forced by the idealized SST over the IO (IDEAL profile above). (c): change in AM3 precipitation (mm day^{-1}) and 925-hPa winds (streamlines) between the reduced meridional gradient run (IDEAL_R) and the idealized run (IDEAL). The black dots in (c) mark the grid points for which the difference in precipitation exceeds the 90% significance level according to the two-tailed Student's t -test.

Figure 6: (a): Observed 200-hPa divergent winds (vectors, m s^{-1}) and convergence ($\times 10^6 \text{ s}^{-1}$) for May. (b): AM3 bias in the 200-hPa divergent circulation for May. (c): latitude-time variation of the AM3 bias in the divergent circulation averaged between (50° - 90°E).

Figure 7: Latitude-time variations of observed (shaded) and AM3 biases (contours) in: (a) precipitation (mm day^{-1} , average between 70° - 100°E); (b): 850-hPa zonal wind (m s^{-1} , average between 55° - 65°E); (c): 200-500-hPa mean temperature anomaly ($^{\circ}\text{C}$, average between 70° - 100°E). The anomaly is calculated by subtracting out the annual and domain average. Data are at pentad resolution.

Figure 8: (a, c, e): Difference in the 174-hPa streamfunction (black contours; $\times 10^{-6} \text{ m}^2 \text{ s}^{-1}$) and 524-hPa pressure-vertical velocity (shades; hPa day^{-1} , positive values represent subsidence) between the control and the reduced heating experiments with the GFDL dry dynamical core model at three different times (from top to bottom, $t = 2, 6, 10$ days, respectively). The vertically-integrated anomalous heating (K day^{-1}) is also represented in (a) as green contours. (b): Difference in the 174-hPa meridional wind (m s^{-1}) at $t = 10$ days. (d): Difference in the vertical-longitude profile of the meridional wind (m s^{-1}) averaged between 26.5° - 35°N and $t = 10$ days (values below orography have been excluded). (f): time-longitude evolution of difference in the 174-hPa meridional wind (m s^{-1}) at 30°N between $t = 1$ day and $t = 12$ days.

Figures

April–May

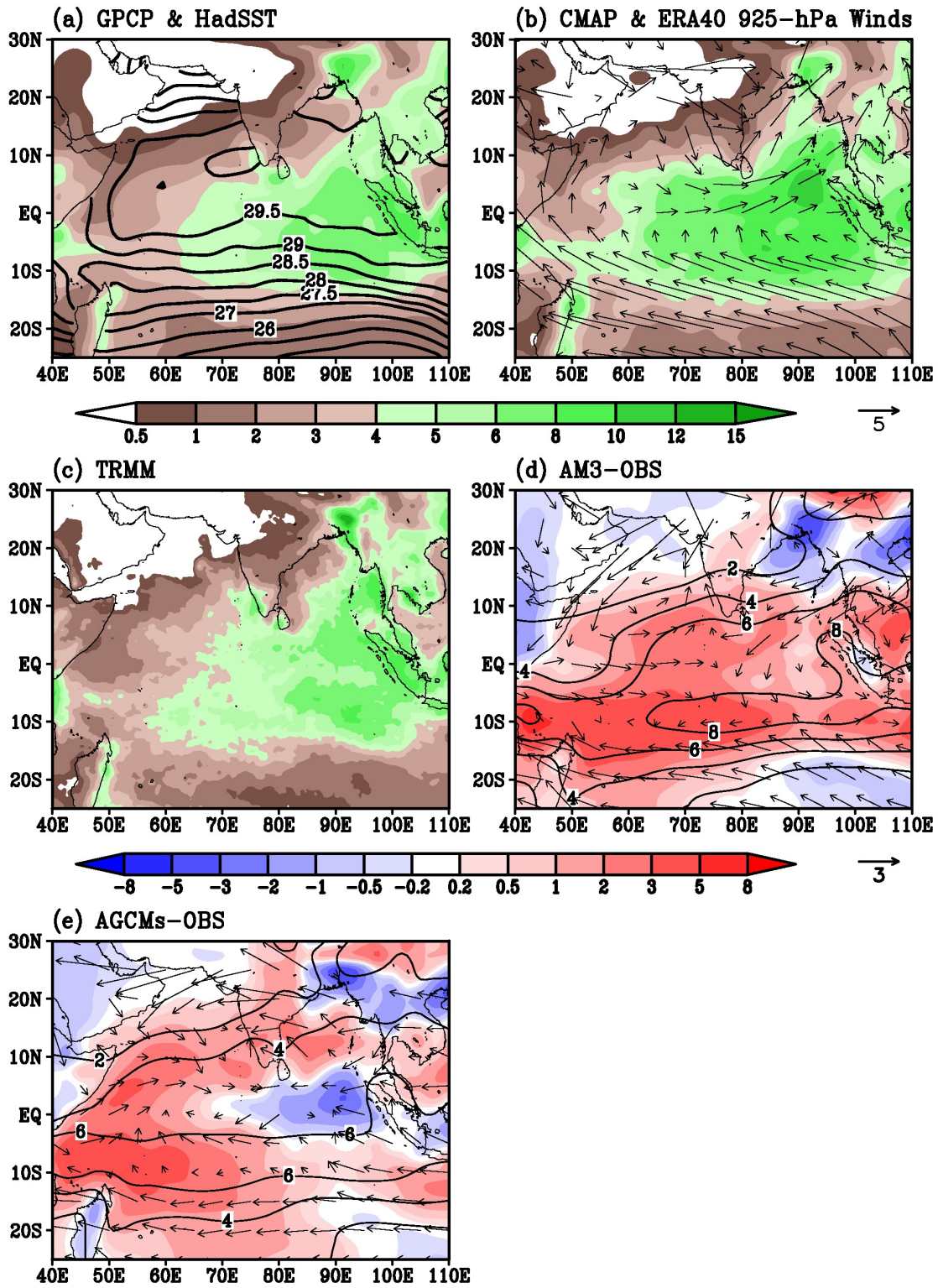


Figure 1: April-May average of: (a) GPCP precipitation (mm day^{-1}) and SST ($^{\circ}\text{C}$); (b) CMAP precipitation (mm day^{-1}) and ERA-40 925-hPa winds (m s^{-1}); (c) TRMM 3B43 precipitation (mm day^{-1}); (d) AM3 biases in precipitation (shaded, mm day^{-1} ; with GPCP as reference) and 925-hPa winds (vectors, m s^{-1}), with the simulated precipitation (mm day^{-1}) as black contours; (e) As (d) but for a multi-model average of five representative AGCMs (i.e., NCAR CAM3, Hadley HadGEM1, MPI ECHAM5, GFDL AM2.1, and CCSR/NIES/FRCGC MIROC3.2 hires) from the IPCC-AR4 archive. All data in (a)-(d) are 1981-2000 mean values, except TRMM which covers the period 1998-2009. Data in (e) are for 1981-1999.

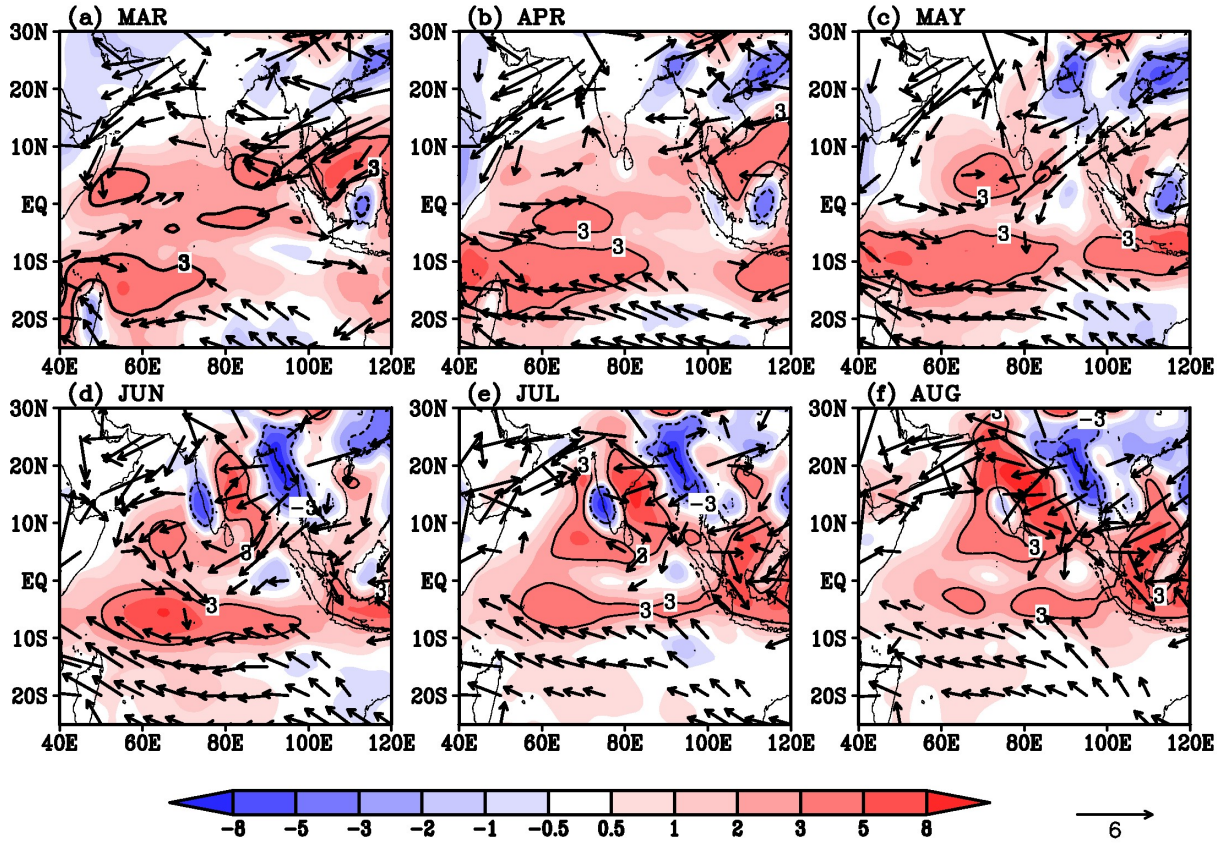


Figure 2: Monthly evolution of the AM3 bias in precipitation (mm day^{-1} , shaded) and 925-hPa winds (m s^{-1} ; vectors plotted only when the magnitude of the wind bias exceeds 1.5 m s^{-1}) from March (a) to August (f).

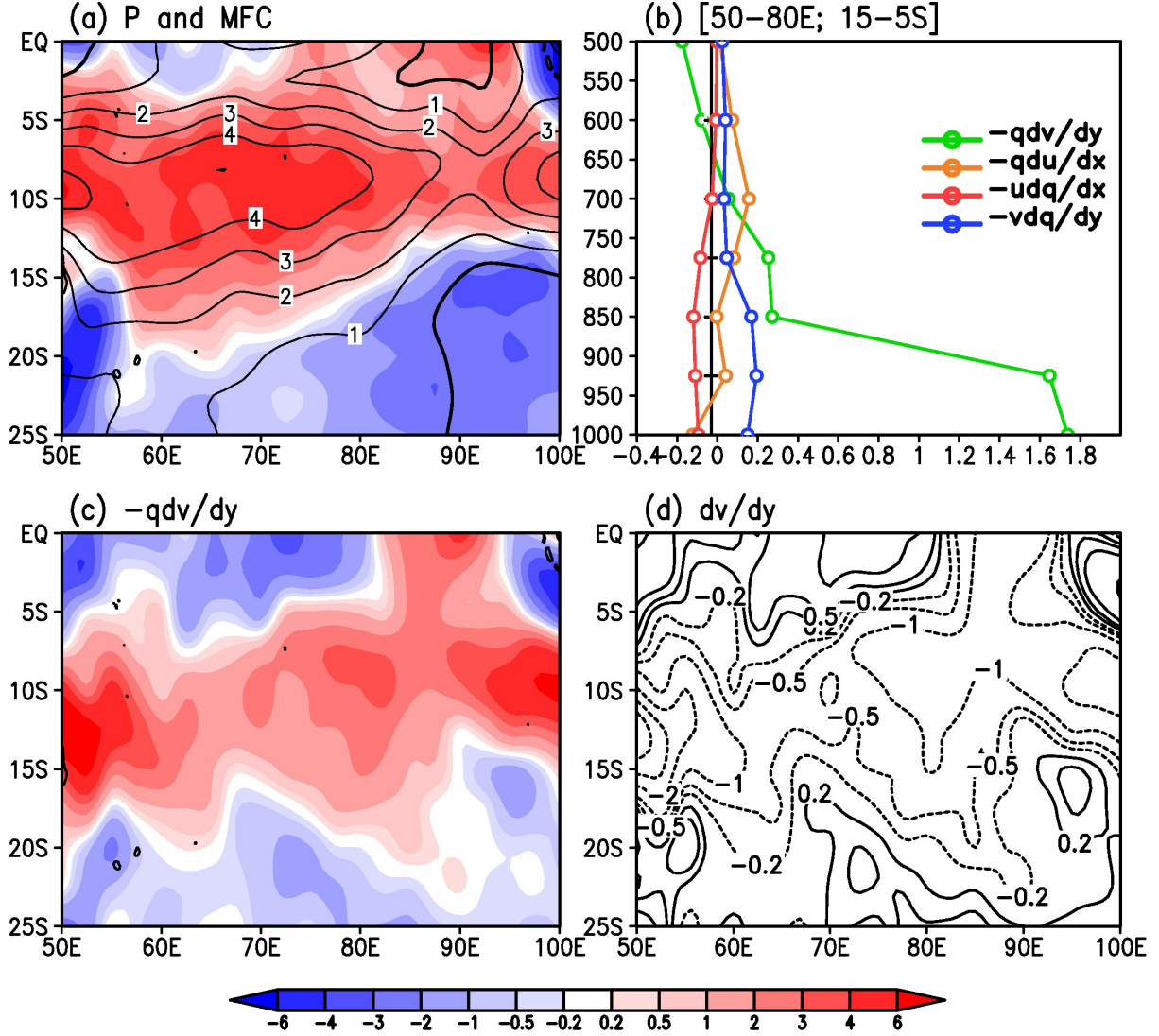


Figure 3: May climatological (a) AM3 bias in precipitation (P , $mm day^{-1}$, contour) and 1000-300 hPa vertically integrated stationary moisture flux convergence (MFC, $mm day^{-1}$, shaded); (b) vertical profiles of the AM3 biases (s^{-1}) in various components contributing to the stationary moisture flux convergence averaged over the area (50° - $80^{\circ}E$, 15° - $5^{\circ}S$); (c) AM3 bias in the 1000-850 hPa vertically integrated meridional moisture transport ($mm day^{-1}$); (d) AM3 bias in the 1000-850-hPa average convergence of the meridional wind ($\times 10^6 s^{-1}$). In these panels, q is specific humidity, v the meridional component of the wind, u the zonal component of the wind, y the latitude, and x the longitude.

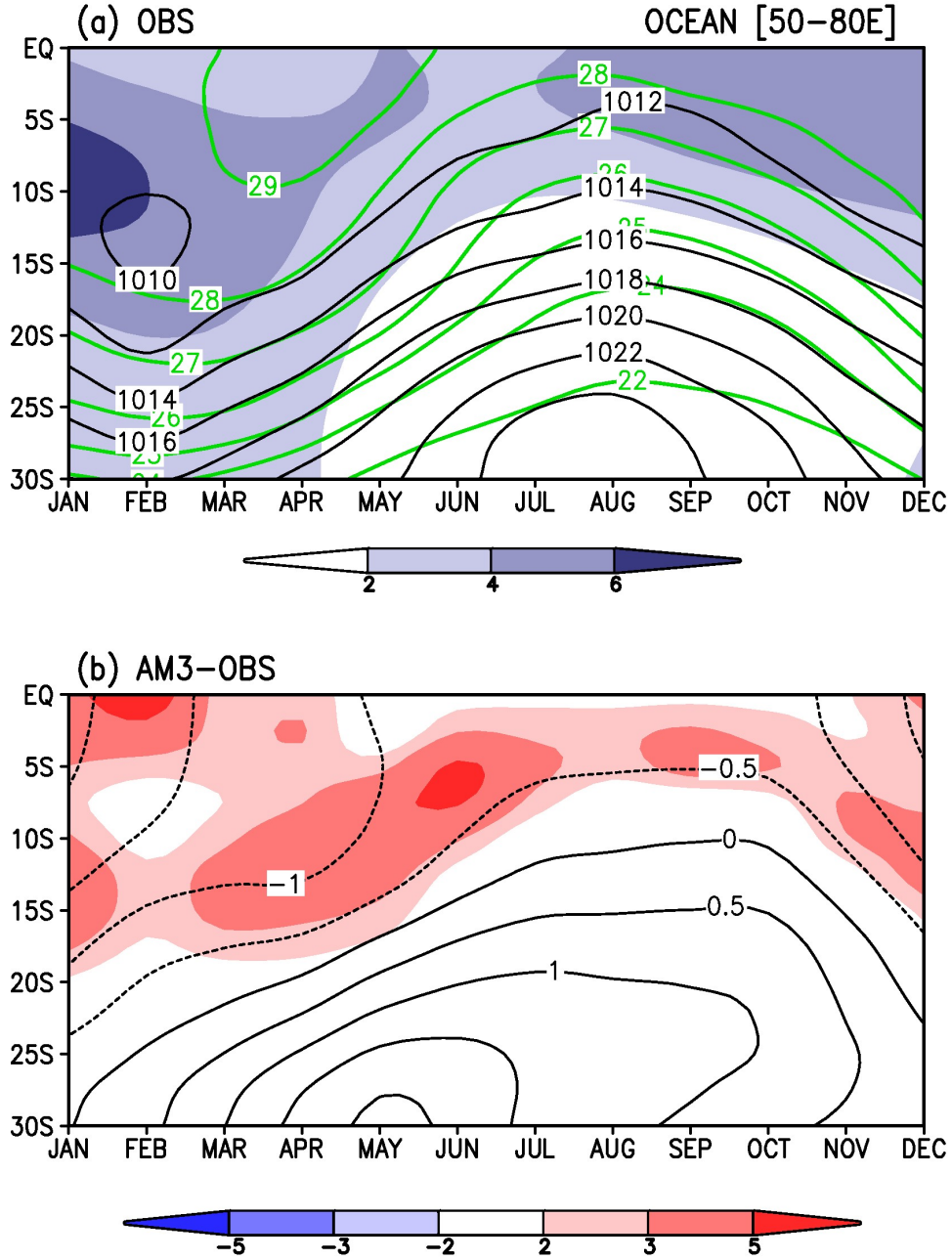


Figure 4: (a): Latitude-time plot of monthly observed GPCP precipitation (mm day^{-1} , shaded), sea level pressure (hPa, black contours), and SST ($^{\circ}\text{C}$, green contours) averaged over the oceanic grid-points between 50°-80°E. (b): as in (a) but for the AM3 bias in precipitation (mm day^{-1} , shaded) and sea level pressure (hPa, black contours).

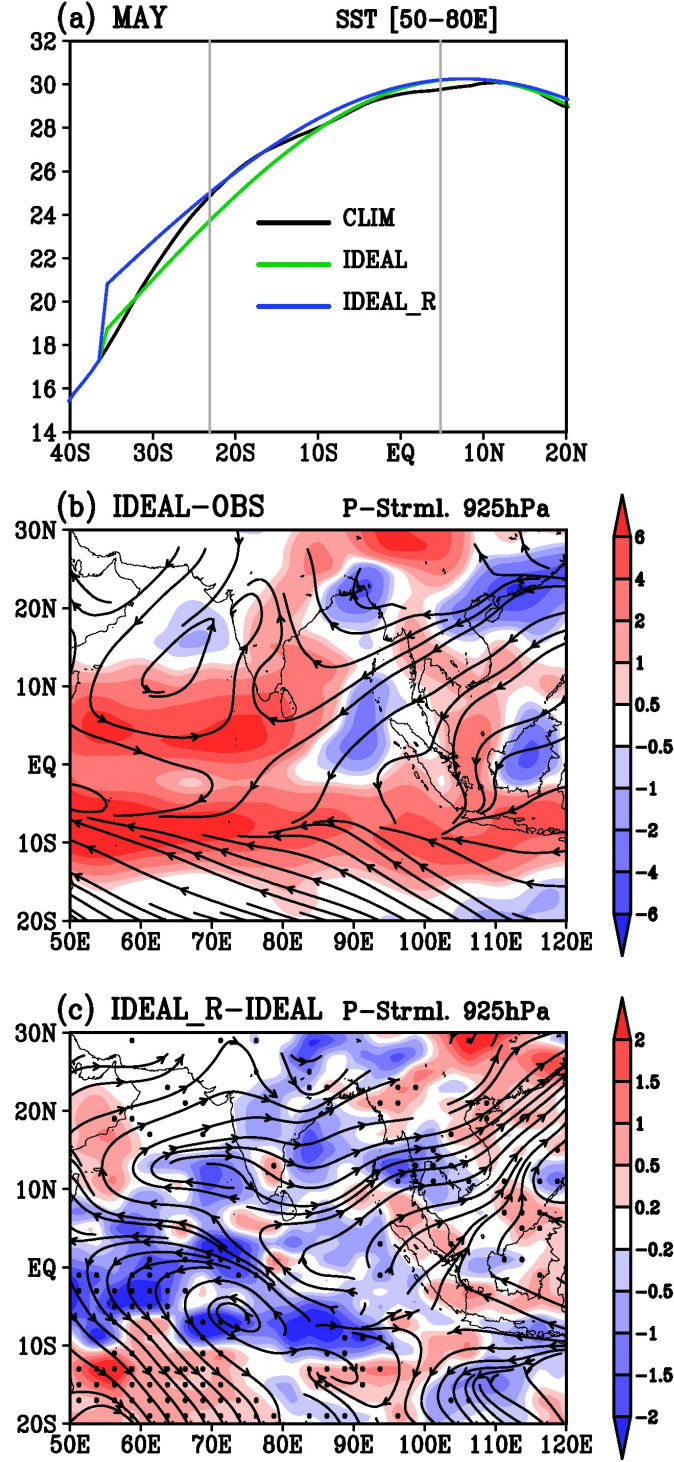


Figure 5: (a): Latitudinal variation of the 50°-80°E average observed May climatological SST (CLIM, black), its Gaussian fit (IDEAL, green), and the Gaussian fit after a 20% reduction of the latitudinal gradient between 23°-5°S (IDEAL_R, blue). (b): AM3 bias in precipitation (shaded, mm day⁻¹) and in 925-hPa winds (streamlines) when forced by the idealized SST over the IO (IDEAL profile above). (c): change in AM3 precipitation (mm day⁻¹) and 925-hPa winds

(streamlines) between the reduced meridional gradient run (IDEAL_R) and the idealized run (IDEAL). The black dots in (c) mark the grid points for which the difference in precipitation exceeds the 90% significance level according to the two-tailed Student's t -test.

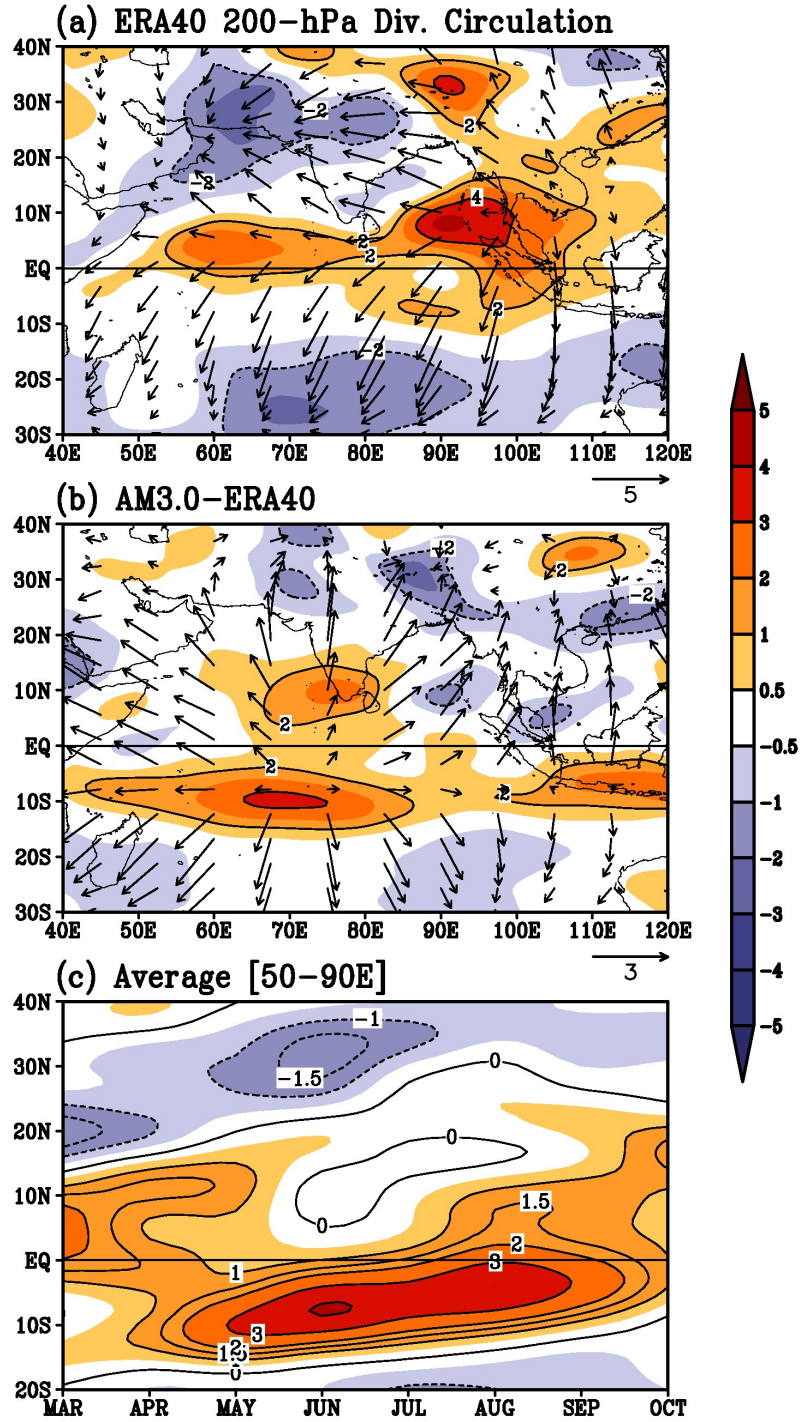


Figure 6: (a): Observed 200-hPa divergent winds (vectors, m s^{-1}) and convergence ($\times 10^6 \text{ s}^{-1}$) for May. (b): AM3 bias in the 200-hPa divergent circulation for May. (c): latitude-time variation of the AM3 bias in the divergent circulation averaged between (50°-90°E).

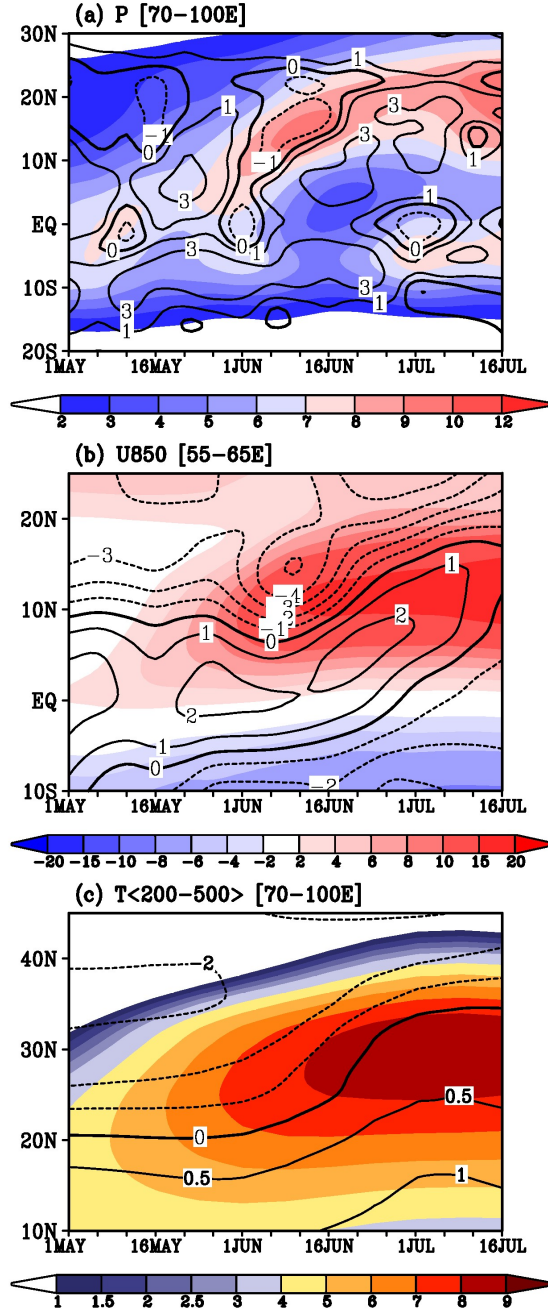


Figure 7: Latitude-time variations of observed (shaded) and AM3 biases (contours) in: (a) precipitation (mm day^{-1} , average between 70° - 100°E); (b) 850-hPa zonal wind (m s^{-1} , average between 55° - 65°E); (c) 200-500-hPa mean temperature anomaly ($^{\circ}\text{C}$, average between 70° - 100°E). The anomaly is calculated by subtracting out the annual and domain average. Data are at pentad resolution.

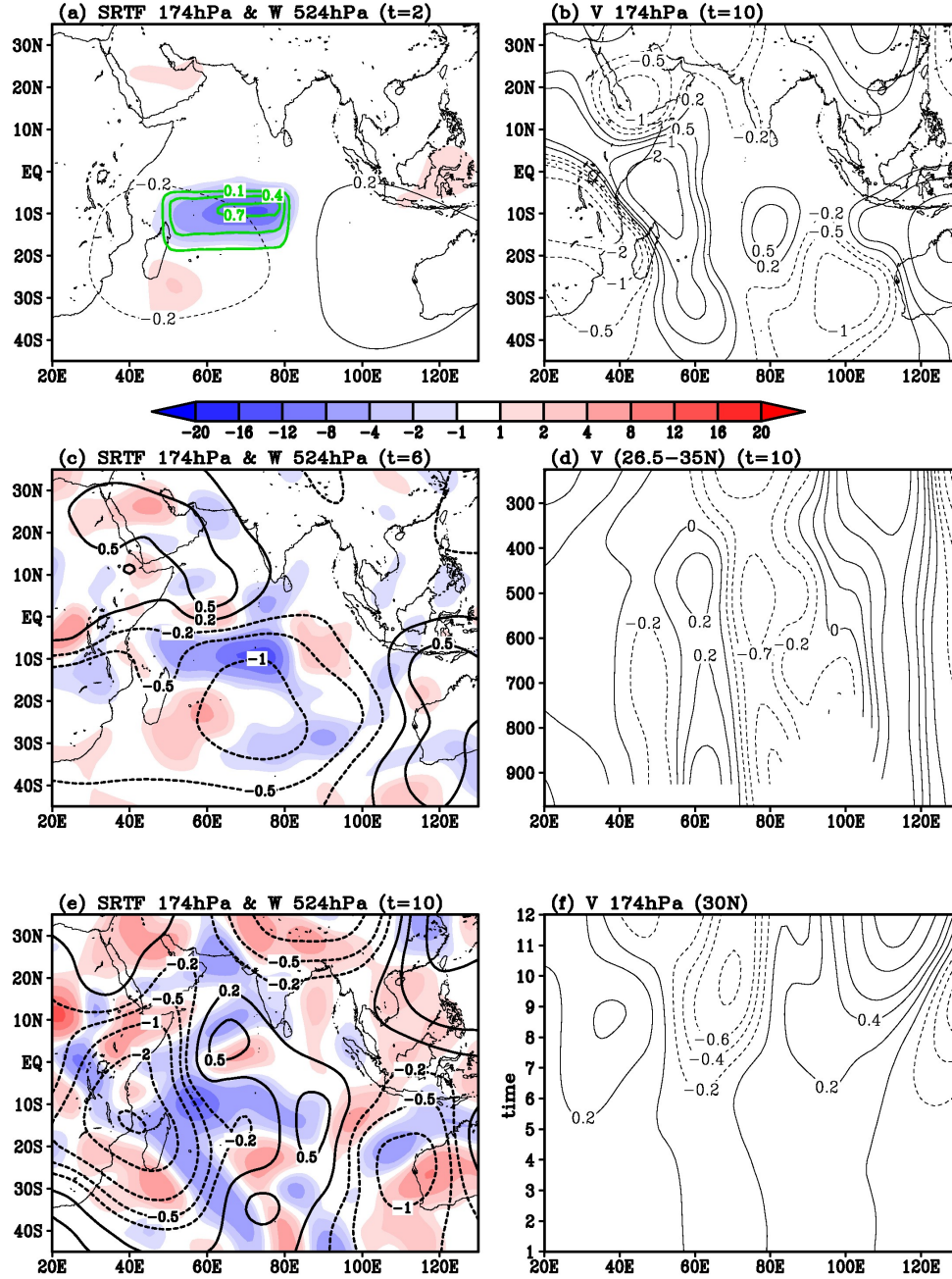


Figure 8: (a, c, e): Difference in the 174-hPa streamfunction (black contours; $\times 10^{-6} \text{ m}^2 \text{ s}^{-1}$) and 524-hPa pressure-vertical velocity (shades; hPa day^{-1} , positive values represent subsidence) between the control and the reduced heating experiments with the GFDL dry dynamical core model at three different times (from top to bottom, $t = 2, 6, 10$ days, respectively). The vertically-integrated anomalous heating (K day^{-1}) is also represented in (a) as green contours. (b): Difference in the 174-hPa meridional wind (m s^{-1}) at $t = 10$ days. (d): Difference in the vertical-longitude profile of the meridional wind (m s^{-1}) averaged between 26.5° - 35°N and $t = 10$ days (values below orography have been excluded). (f): time-longitude evolution of difference in the 174-hPa meridional wind (m s^{-1}) at 30°N between $t = 1$ day and $t = 12$ days.